Effect of Pr, Mn Doping on the Structure and Properties of $BiFeO_3$

Lei Zhou
Shanghai Institute of Technology
Guojian Jiang (guojianjiang@sit.edu.cn)
Shanghai Institute of Technology https://orcid.org/0000-0001-8290-8925
Dandan Wu
Shanghai Institute of Technology
Jianbing Chen
Shanghai Institute of Technology

Research Article

Keywords: BiFeO3, Pr, Mn doping, Hydrothermal method, Magnetism

Posted Date: February 18th, 2021

DOI: https://doi.org/10.21203/rs.3.rs-188721/v1

Abstract

The powders of Bi1-xPrxFeO3 (x = 0, 0.05, 0.1) and Bi0.95Pr0.05Fe1-yMnyO3 (y = 0.05, 0.1) were prepared by hydrothermal method. The effects of Pr and Mn doping content on the structure, morphology, magnetic, and photocatalytic properties of $BiFeO_3$ (BFO) have been studied. X-ray diffraction (XRD) demonstrated that the compounds are distorted rhombohedral perovskite structure without any other heterogeneity and structural transition. Field emission scanning electron microscope (FESEM) reflected that the surface of compounds is a dense, agglomerated sphere, and the morphology changes with the addition of Pr, Mn. Energy spectrum analysis (EDS) shows that the $Bi_{0.95}Pr_{0.05}Fe_{0.95}Mn_{0.05}O_3$ sample is mainly composed of 5 elements (Bi, Fe, O, Pr, Mn), and the atomic ratio matches the formula well. Integrating the vibrating sample magnetometer (VSM) into the physical property measurement system (PPMS-9) shows that the introduction of $Pr^{3+}$and Mn^{2+} ions can enhance the magnetic properties of BFO at room temperature. In addition, doping with Pr^{3+} and Mn^{2+} ions can improve the photocatalytic performance of BFO, and with the increase of Mn^{2+} concentration, the photocatalytic performance of BFO first rises and then decreases, and its catalytic performance is getting better and better.

Relevance Summary

- By co-doping BFO with Pr and Mn, the distortion of crystal structure was caused, the spiral structure of BFO was broken, and the magnetic energy was improved.
- Current studies mainly focus on the magnetic ion doping of BiFeO3, this paper explores the non-magnetic ion doping of BiFeO3
- The magnetic and photocatalytic properties of $BiFeO_3$ powders co-doped with magnetic and non-magnetic ions were studied, and the appropriate doping amount was determined.

1. Introduction

Multiferroic materials are a typical representative of multifunctional materials, combined electricity and magnetism. The research of multi-ferrous materials belongs to international hotspots, and it is also a basic frontier scientific issue with application traction, which involves the fields of materials, physics, chemistry, etc. At present, material science and condensed matter physics is a broad new field, which contains a wealth of research topics in material science and physics and has a wide range of application prospects. The research of multi-ferrous $BiFeO_3$ is one of the most representative single-phase multi-iron materials, and the perovskite structure belongs to the R3c space group. It is one of the few materials that has both ferroelectric and antiferromagnetic properties at room temperature, with high ferroelectric Curie temperature (850 °C) and ferromagnetic Neel temperature (370 °C), as well as narrow forbidden bandwidth and better Chemical stability, etc. These excellent properties make it suitable for applications such as magneto-optical devices [1], information storage [2], sensors [3], nanogenerators [4], and catalysts [5].

However, as $BiFeO_3$ is caused by the spatial periodic non-uniform spin structure, he properties of weak magnetism limit its practical application. At the same time, BFO is also a typical narrow bandgap semiconductor, which can respond to the visible range that TiO_2 cannot respond to. So that it can exhibit excellent chemical stability in the visible light photocatalysis process [6]. However, pure BFO exhibits poor photocatalytic activity because of the rapid recombination of photogenerated electrons, and holes.

Over the years, scholars at home and abroad have been working on improving the performance of BFO. Among them, ion doping is the most widely studied method. Ion doping of A, B, and AB was used to improve the performance of BFO. The A site is mainly rare earth elements (La[7-8], Nd[9-10], Sm[11-13], Pr[7, 12]), mainly because its ionic radius and valence are similar to those of Bi^{3+}, and it is easy to dope to replace Bi ions and inhibit the volatilization of Bi. The B site is mainly doped with transition metal ions (Cr, Co, Mn) [14]. Doping magnetic ions at the B site can inhibit the valence state of iron and destroy the super-exchange effect in the spin-helical structure of BFO. Therefore, the magnetic performance is enhanced. Meantime, ion doping is an effective method to the increase photocatalytic activity of BFO [15]. Zhang et al. [16] prepared different Gd-doped BFO thin films by sol-gel method. The effect of Gd doping on the catalytic activity of BFO thin films was studied. The research shows that proper Gd doping can increase the photocatalytic activity of the thin films. Gd doping increases light absorption, can effectively separate the migration of photogenerated carriers and reduce the recombination probability of electron-holes. At the same time, because BFO has weak ferromagnetism, it can be recovered from water contaminants by external magnets for recycling.

The AB-doping can be the advantage of combining the two to get a better modification effect [17]. Pr-doped BFO and Pr, Ti co-doped BFO were prepared by solid-state reaction. The study found that both the single or double doping properties were obtained and the magnetic properties of the double doping were more pronounced. The reason is that the antiferromagnetic transition temperature (TN) decreases as the doping concentration increases, and the transition temperature is 354 °C when x=0.20. The net magnetization of the doped to sample increased significantly, indicating that non-magnetically active Ti^{4+} ions were added at the magnetic Fe^{3+} site, which destroyed the Fe-O-Fe network and formed the AFM-type sublattice spin ring [18]. By the way, according to reports in ion-doped BFO, low-cost ion doping can introduce negatively charged defects, which can effectively suppress the price change of Fe^{3+}. Therefore, it is associated with the study of Prions and low-value ion-doped BFO.

In this work, pure BFO and Pr, and Mn-doped BFO have been synthesized by the hydrothermal method. Compared with other methods, the hydrothermal method is easy to control, the reaction time is short, and the synthetic sample has high purity. Also, the structure, magnetic and photocatalytic activity of Pr^{3+} and low-cost Mn^{2+} co-doped BFO have been studied in detail, which have not been reported in detail so far.

2. Experimental

The powders of BFO and $Bi_{1-x}Pr_xFe_{1-y}Mn_yO_3$(x=0, 0.05, 0.10 y=0.05, 0.10) were prepared by a hydrothermal method. The raw materials required for the experiment were $Bi(NO_3)_3·5H_2O$, $Fe(NO_3)_3·9H_2O$, $Pr(NO_3)_3·6H_2O$, $C_4H_6MnO_4$ and KOH. First, the proper concentration of KOH solution is prepared, and then the other raw materials are successively added to the KOH solution, and then stirred for 30 minutes, waiting for the raw materials to completely dissolve. Then the prepared solution was ultrasonic in the ultrasonic machine for 20 minutes, and then stirred for 40 minutes, and poured into the reactor. Finally, after heated at 200℃ for 24 h, the powders was repeatedly washed with deionized water, and then dried at 60℃ for 6h to get the final powders

The phase compositions of the powders was analyzed by X-ray diffraction (Bruker D8) with Cu Kα (λ=1.5406 Å) radiation. The surface morphology of the powders was observed by scanning electron microscopy (Gemini SEM 300, Zeiss, Germany). The elemental analysis of the powders was observed by energy-dispersive X-ray spectroscope (EDX). The magnetic measurement of the powders was checked by a physical property measurement system (PPMS-9, Quantum Design). The UV-visible absorption spectroscopy of the powders was recorded at room temperature with Agilent Cary-5000.

The photocatalytic performance of the sample is usually tested by adding the sample to the methylene blue (MB) solution and irradiating it under the xenon lamp. The photocatalytic performance of the sample is determined by measuring the absorbance of the solution at different times. The 0.5 g sample and 100 mL methylene blue (MB) solution concentration (0.1mg/ mL) were first placed in a reactor, stirred in the dark for 30 minutes, and then irradiated under a xenon lamp. Samples were taken every 30min to measure the absorbance of the solution..

3. Results And Discussion

Figure 1a shows the XRD pattern of $Bi_{1-x}Pr_xFe_{1-y}Mn_yO_3$($0 \leqq x \leqq 1$, $0 \leqq y \leqq 1$) powders. It can be seen that the diffraction peaks of all the samples are strong and sharp, indicating that the crystallinity of the batch sample is good. The XRD pattern of $Bi_{1-x}Pr_xFe_{1-y}Mn_yO_3$ ($0 \leqq x \leqq 1$, $0 \leqq y \leqq 1$) match well with the standard card of $BiFeO_3$ (JCPDS No. 71-2494), and there is no heterogenic peak of Bi_2O_3. The XRD pattern of all the samples confirmed that the rhombohedral perovskite structure have R3C space group. Moreover, When Pr doped BFO alone, with the increase of Pr doping concentration, the XRD diffraction peak shifted to a low angle; when Pr and Mn co-doped BFO, with the increase of Mn doping concentration, the XRD diffraction peak shifted to a higher angle offset. As shown in Figure1b, the (104) and (110) peaks of Pr single-doped BFO move to the left, and the peaks of Pr and Mn co-doped shift to the right. This is because the radius of Pr^{3+} is larger than the radius of Bi^{3+}, and the radius of Mn^{2+} is smaller than the radius of Fe^{3+}. At the same time, the average grain size of all doped and undoped samples was calculated using the Scherrer formula:

$$D=\frac{k\lambda}{\beta\cos\theta}$$

Where k = 0.89 is the shape factor, λ is the wavelength of the x-ray λ = 0.15405 nm, β is the full width at half maximum, θ is the diffraction angle, and D is the crystallite size.

It is observed from Table 1 that the average grain size of the BFO sample varies from 41 nm to 28 nm with the increase of Pr single doping and the concentration of Pr and Mn co-doping. With the increase of single-doped Pr concentration, the lattice parameters increase, thus resulting in a larger volume. While with the increase of Mn concentration, the lattice parameters of Pr, Mn co-doped BFO decrease slightly, and the volume shrinks. This may be due to the difference in ionic radius between Pr and Bi, as well as Mn and Fe. These results indicate that Pr and Mn can be effectively introduced into the crystal structure of BFO

Table 1 Structure parameters of BFO and $Bi_{1-x}Pr_xFe_{1-y}Mn_yO_3$(x=0, 0.05, 0.10 y=0.05, 0.10)

Composition	Lattice constant		Grain size	Volume
x	a/ Å	c/ Å		V/ Å
BFO	5.58756±0.00323	13.84247±0.006194	41.06	373.27
BPFO x=0.05	5.62797±0.006375	13.83428±0.012529	41.56	379.48
BPFO x=0.10	5.62838 ±0.00911	13.97317±0.032953	41.67	383.35
BPFMO y=0.05	5.62192±0.00657	13.95784±0.018818	39.89	382.05
BPFMO y=0.10	5.6263±0.008675	13.91666±0.026479	28.18	381.52

Figure 2 show the SEM images of BFO, $Bi_{0.95}Pr_{0.05}FeO_3$ and $Bi_{0.95}Pr_{0.05}Fe_{0.95}Mn_{0.05}O_3$ powders. Their morphology and size were observed by FESEM and the results are shown in Figure 2a. It can be seen that the pure phase BFO powder presents a regular polyhedral morphology, which is a condensed spherical morphology composed of many fine crystal grains. Figure 2b and 2c shows the microstructure of Pr-doped and Pr, Mn-doped BFO crystallites become rougher than that of BFO, and the surface of the $Bi_{0.95}Pr0.05Fe_{0.95}Mn_{0.05}O_3$ sample has stratification. Meanwhile, the EDS analysis in Figure 2d showed that the Bi0.95Pr0.05Fe0.95Mn0.05O3 sample mainly consists of five elements (Bi, Fe, O, Pr, Mn) and atom ratio matched well with the formula.

Figure 3 shows the infrared absorption spectra of $Bi_{1-x}Pr_xFeO_3$ (x = 0, 0.05, 0.1), $Bi_{0.95}Pr_{0.05}Fe_{1-y}Mn_yO_3$ (y = 0.05, 0.1) samples recorded in the range of 400-800 cm^{-1} at room temperature. For the ideal perovskite

structure, there are three kinds of vibration, stretching, bending, and lattice vibration of the infrared spectrum. As shown in Figure 3, two peaks can be observed at 400-600 cm^{-1}, which was caused by the stretching vibration of Fe-O and the bending vibration of O-Fe-O. It is generally believed that the vibration near 560 cm^{-1} corresponds to the tensile vibration of Fe-O-Fe. The Fe-O-fe bond length is very sensitive and corresponds to the Fe-O stretching vibration of the FeO6 octahedron. The vibration at 425 cm^{-1} is a flexural vibration sensitive to the Fe-O-fe bond angle, which corresponds to the Fe-O flexural vibration of FeO6 octahedron [19-20]. Moreover, It can be seen that with the concentration of Prions and Mn ions increase, the infrared spectrum has a significant red shift, which is mainly due to the high peak of the infrared absorption spectrum caused by the radius of Pr^{3+} radius larger than Bi^{3+}. At the same time, the absorption peak of tensile vibration gradually widens until it disappears. There is almost no change in the absorption peak of flexural vibration, indicating that Mn doping causes the bond length to change, but the bond angle does not change much.

Figure 4 shows the hysteresis loops of BFO, $Bi_{1-x}Pr_xFeO_3$ (x = 0.05, 0.1) and $Bi_{0.95}Pr_{0.05}Fe_{1-y}Mn_yO_3$ (y = 0.05, 0.1) samples tested at room temperature by PPMS-9 with a maximum magnetic field of 6T. It can be seen that the pure-phase BFO exhibits typical antiferromagnetic behavior, the nonlinearity of M (H) is very small, there is no remanence, the coercive force is almost zero, and it shows a linear loop under the action of an external magnetic field. The hysteresis loops of all samples did not reach saturation. In the case of Pr^{3+} single-doped BFO, the addition of a small amount of Pr^{3+} does not fundamentally change the direction of the magnetization curve, and the magnetization increases with the doping amount of Pr^{3+}, except the Pr^{3+} doping amount is 5%. This shows that Pr doping can improve magnetic properties but requires a minimum doping amount. This may be due to the excessive substitution of Bi^{3+} by Pr^{3+}, which reduces the oxygen vacancies caused by the volatilization of Bi^{3+}. On the other hand, the introduction of Pr^{3+} leads to the coupling of the magnetic moment between Pr^{3+}-Fe^{3+}, which can destroy the antiferromagnetic structure of BFO then enhance the magnetic of the sample. When Pr and Mn are co-doped, the magnetic properties can also be enhanced by increasing the amount of Mn doping, because Mn^{2+} is a magnetic ion, doping makes the magnetic property increase. The FeO_6 octahedron would be distorted as the doping of Mn ion, thus changes the helical antiferromagnetic structure of BFO then resulting in a new Fe-O-Mn network structure and making the interaction between Fe-Mn stronger.

The photocatalytic activity of BFO and $Bi_{0.95}Pr_{0.05}Fe_{1-x}Mn_xO_3$ (x=0, 0.05, 0.1) samples was investigated by photocatalytic degradation of methylene blue (MB) under visible light irradiation. Figure 5 show the relationship between the concentration and time of MB degradation by visible light simulated by 500W xenon lamp. It can be clearly seen that with the increase of visible light irradiation time, the main absorption peak decreases rapidly, illustrating the obvious catalytic activity of $Bi_{0.95}Pr_{0.05}Fe_{0.95}Mn_{0.05}O_3$ compounds for the degradation of MB under visible light irradiation. Figure 5b the shows change of photodegradation rate for BFO and $Bi_{0.95}Pr_{0.05}Fe_{1-x}Mn_xO_3$ (x=0, 0.05, 0.10) photocatalysts with illumination time. The results show that the degradation rate of $Bi_{0.95}Pr_{0.05}FeO_3$ within 120 min is 70%, which is better than BFO. At the same time, the photocatalytic activity of Pr and Mn co-doped BFO

increased with the increase of Mn^{2+} concentration. It can be seen from Figure 5b that after 120 minutes of reaction, when x = 0.10, the photocatalytic efficiency of the sample reaches 85%, indicating that the catalytic activity of doped Mn^{2+} is significantly enhanced. The reason for the improved photocatalytic activity may be that the introduction of Mn^{2+} has increased the deformation and surface defects of FeO_6 octahedrons, thereby rapidly recombining the holes and electrons of the corrosion inhibitor, and increasing the concentration of active centers, thereby improving the catalytic performance. Therefore, Pr and Mn co-doped BFO can improve the catalytic performance of BFO by promoting the generation of electron-hole pairs.

4. Conclusion

In this work，the samples of pure phase BFO, Pr-doped BFO and Pr, Mn co-doped BFO were prepared by hydrothermal method The structure is rhombohedral perovskite structure, space group is R3c, and without impurity phase, BFO, $Bi_{1-x}Pr_xFeO_3$ (x=0.05, 0.1) and $Bi_{0.95}Pr_{0.05}Fe_{1-y}Mn_yO_3$ (y=0.05, 0.1) samples are all pure phase. When Pr is doped into BFO, the magnetic properties decrease first and then increase with the amount of Pr doping. It is stated that there is a limit on the minimum doping amount for Pr single doping. When Pr, Mn is co-doped, the magnetic properties increase with the amount of Mn^{2+} doping. This is mainly since Mn^{2+} is a magnetic ion, and its addition contributes to ferromagnetism. The formation of a new network structure can change the spin-helical structure of BFO and improved the magnetic properties. In terms of photocatalysis, the catalytic efficiency could be improved as the increase of Mn^{2+} doped amount, which speculated that the photocatalytic effect would be better when the doping amount of Mn^{2+} continuously increased. In this work, it is found that Pr and Mn co-doped BFO can not only improve the magnetic properties of BFO but also improve its catalytic performance. Therefore, the doping of BFO has a good application prospect for both magnetism and optics. properties which are mainly related to the super-exchange of Fe-O-Fe.

Declarations

Acknowledgments

This work is supported by the State Key Lab of Advanced Metal Materials open Research fund (2020-Z02), State Key Laboratory of Silicon Materials, Zhejiang University (SKL2020-04), Shanghai Science and Technology Commission (19DZ2332000)

Funding: This work is supported by the State Key Lab of Advanced Metal Materials open Research fund, State Key Laboratory of Silicon Materials, Zhejiang University, Shanghai Science and Technology Commission.

Conflicts of interest/Competing interests: The authors declare no conflict of interest. We declare that we do not have any commercial or associative interest that represents a conflict of interest in connection with the work submitted.

Availability of data and material: Some or all data, models, or code generated or used during the study are available in a repository or online in accordance with funder data retention policies (Provide full citations that include URLs or DOIs.).

Code availability: origin8

Authors' contributions: Lei Zhou: Roles/Writing - original draft; Investigation; Methodology

Guojian Jiang: Review & editing, Dandan Wu: Resources; Writing - review & editing, Jianbing Chen: Validation

References

1. C. Michel, J. M. Moreau, G. D. Achenbach, R. Gerson, and W. J. James, Solid State Commun. **7**, 701 (1969).
2. R. Karthick and R. Srinivasan, J. Magn. Magn. Mater. **441**, 443 (2017).
3. M. Bibes and A. Barthélémy, Nat. Mater. **7**, 425 (2008).
4. X. Liu, B. Cheng, J. Hu, H. Qin, and M. Jiang, Sensors Actuators, B Chem. **133**, 340 (2008).
5. X. Wang, J. Song, J. Liu, and L. W. Zhong, Science. **316**, 102 (2007).
6. C. M. Raghavan, J. W. Kim, and S. S. Kim, Ceram. Int. **39**, 3563 (2013).
7. G. L. Yuan, K. Z. Baba-Kishi, J. M. Liu, S. W. Or, Y. P. Wang, and Z. G. Liu, J. Am. Ceram. Soc. **89**, 3136 (2006).
8. Y. I. Golovko, V. M. Mukhortov, O. A. Bunina, I. N. Zakharchenko, A. S. Anokhin, V. B. Shirokov, and Y. I. Yuzyuk, Phys. Solid State **52**, 1432 (2010).
9. K. S. Nalwa, A. Garg, and A. Upadhyaya, Mater. Lett. **62**, 878 (2008).
10. S. K. Pradhan and B. K. Roul, J. Phys. Chem. Solids **72**, 1180 (2011).
11. Y. P. Liu and J. M. Wu, Electrochem. Solid-State Lett. **10**, 39 (2007).
12. J. B. Li, G. H. Rao, J. K. Liang, Y. H. Liu, J. Luo, and J. R. Chen, Appl. Phys. Lett. **90**, 1 (2007).
13. B. Yu, M. Li, Z. Hu, L. Pei, D. Guo, X. Zhao, and S. Dong, Appl. Phys. Lett. **93**, 1 (2008).
14. V. A. Khomchenko, D. A. Kiselev, I. K. Bdikin, V. V. Shvartsman, P. Borisov, W. Kleemann, J. M. Vieira, and A. L. Kholkin, Appl. Phys. Lett. **93**, 1 (2008).
15. H. Wu, P. Xue, Y. Lu, and X. Zhu, J. Alloys Compd. **731**, 471 (2018).
16. N. Zhang, D. Chen, F. Niu, S. Wang, L. Qin, and Y. Huang, Sci. Rep. **6**, 1 (2016).
17. S. Chandel, P. Thakur, S. S. Thakur, V. Kanwar, M. Tomar, V. Gupta, and A. Thakur, Ceram. Int. **44**, 4711 (2018).
18. J. Zhang, B. J. Wang, X. Ju, T. Liu, and T. D. Hu, Polymer (Guildf). **42**, 3697 (2001).
19. R. K. Mishra, D. K. Pradhan, R. N. P. Choudhary, and A. Banerjee, J. Magn. Magn. Mater. **320**, 2602 (2008).

20. A. Ianculescu, F. P. Gheorghiu, P. Postolache, O. Oprea, and L. Mitoseriu, J. Alloys Compd. **504**, 420 (2010)

Figures

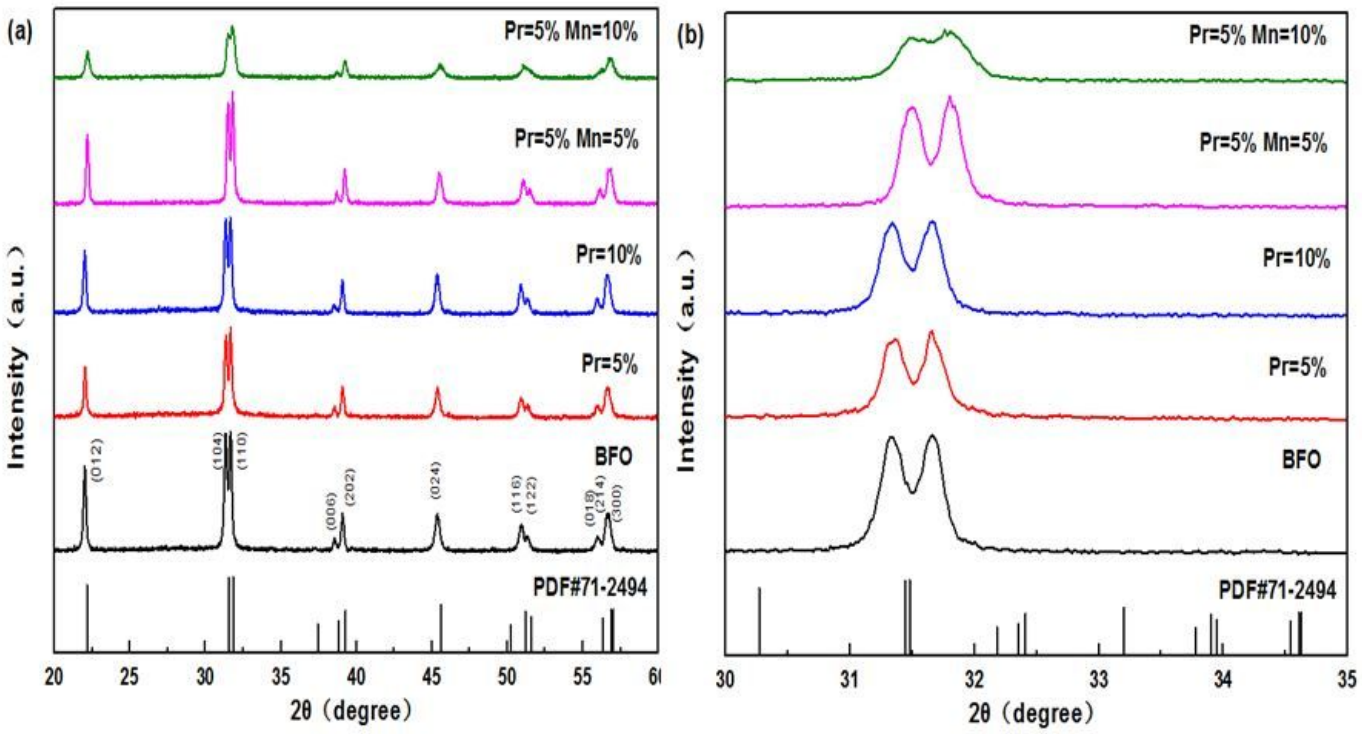

Figure 1

XRD patterns of the Bi1-xPrxFe1-yMnyO3(x=0, 0.05, 0.10 y=0.05, 0.10) powers

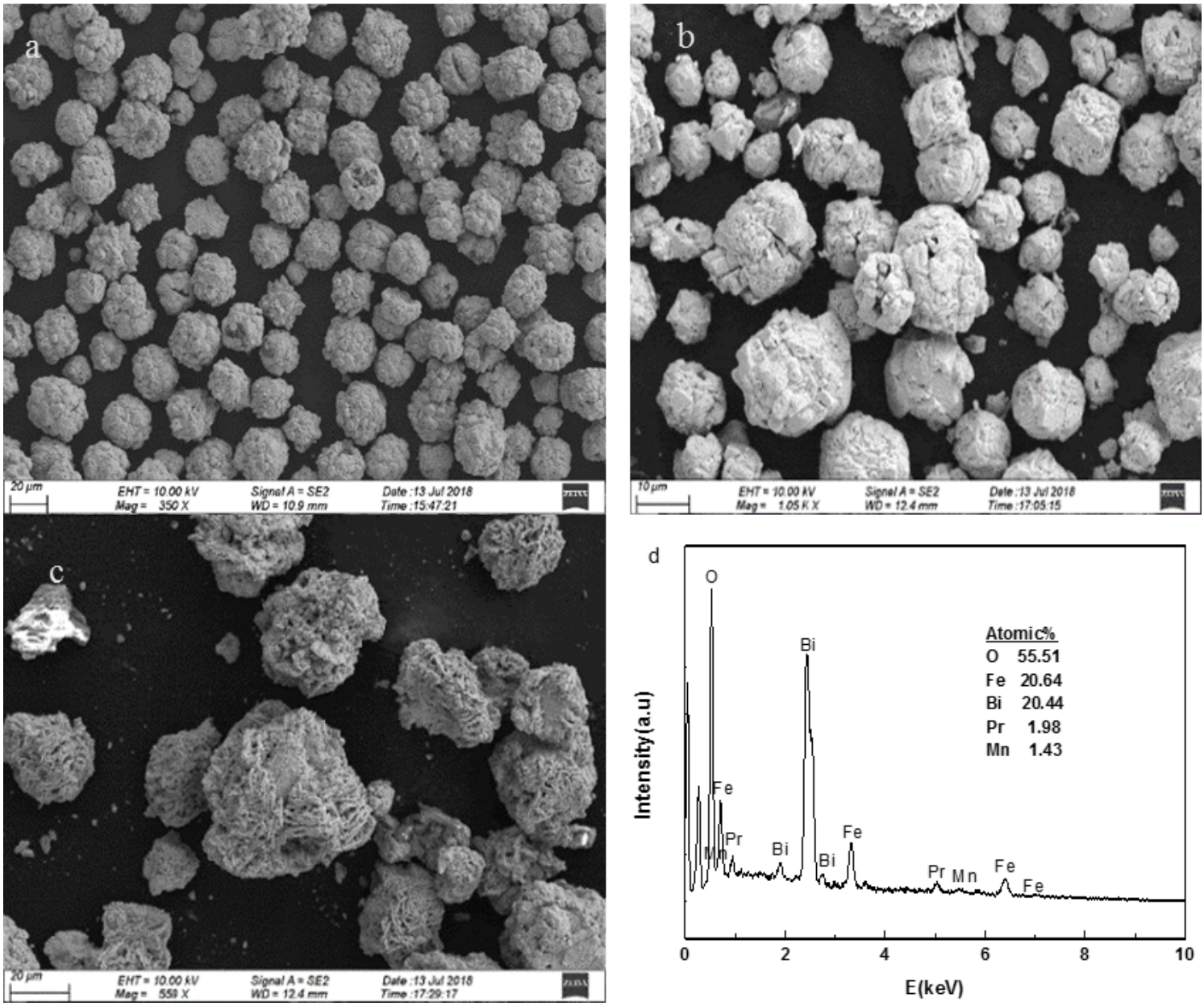

Figure 2

SEM images of BFO (a), Bi0.95Pr0.05FeO3 (b), and Bi0.95Pr0.05Fe0.95Mn0.05O3 (c); EDS analysis of Bi0.95Pr0.05Fe0.95Mn0.05O3 sample (d)

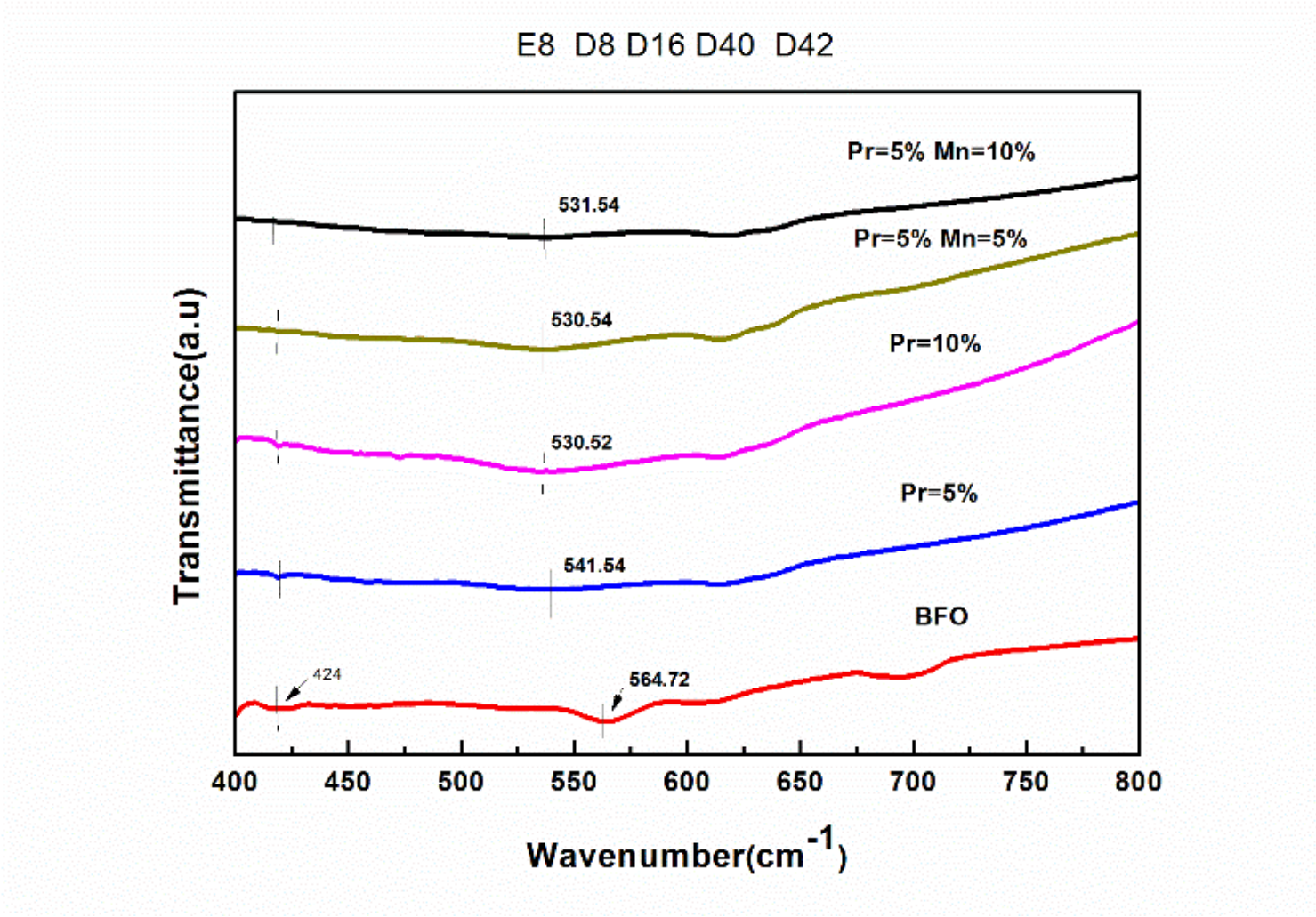

Figure 3

FTIR spectra of BFO, Bi1-xPrxFeO3 (x=0.05, 0.1), Bi0.95Pr0.05Fe1-yMnyO3 (y=0.05, 0.1)

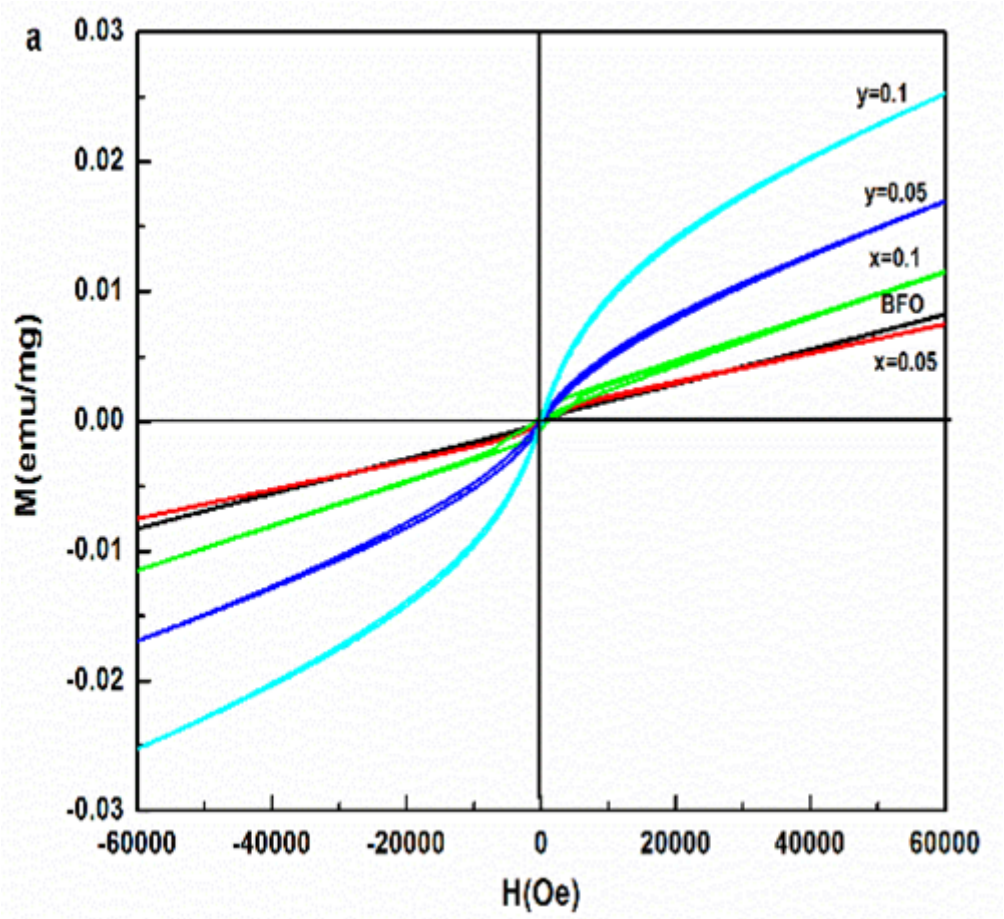

Figure 4

Field dependence of magnetization of BFO, Bi1-xPrxFeO3 (x=0.05, 0.1) and Bi0.95Pr0.05Fe1-yMnyO3 (y=0.05, 0.1) at room temperature

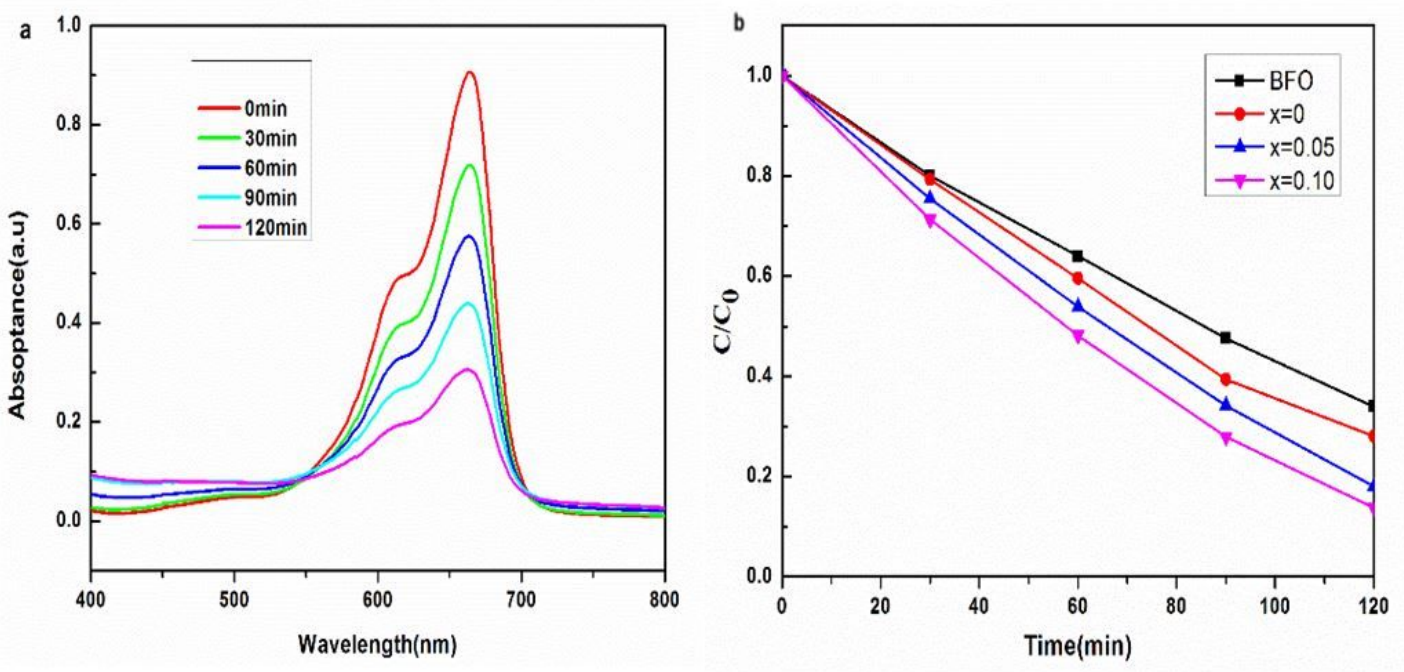

Figure 5

(a) UV-Vis Spectra of Bi0.95Pr0.05Fe0.95Mn0.05O3 Catalyzed Photodegradation of MB; (b) Photocatalytic performance of BFO and Bi0.95Pr0.05Fe1-xMnxO3 (x=0, 0.05 0.10) samples degrading MB under visible light irradiation